Analytical calculation of the *Q* factor for circular-grating microcavities

Asma Jebali

Communication Photonics Group, Laboratory for Electromagnetic Fields and Microwave Electronics, ETH Zurich, 8092 Zurich, Switzerland, and IBM Research, Zurich Research Laboratory, Säumerstrasse 4, 8803 Rüschlikon, Switzerland

Daniel Erni

Communication Photonics Group, Laboratory for Electromagnetic Fields and Microwave Electronics, ETH Zurich, 8092 Zurich, Switzerland and Department of Electrical Engineering (ATE), Faculty of Engineering, University of Duisburg-Essen, Bismarckstrasse 81, 47057 Duisburg, Germany

Stephan Gulde

Institute of Quantum Electronics, ETH Zurich, 8093 Zurich, Switzerland

Rainer F. Mahrt

IBM Research, Zurich Research Laboratory, Säumerstrasse 4, 8803 Rüschlikon, Switzerland

Werner Bächtold

Laboratory for Electromagnetic Fields and Microwave Electronics, ETH Zurich, 8092 Zurich, Switzerland

Received May 5, 2006; revised October 31, 2006; accepted November 13, 2006; posted November 15, 2006 (Doc. ID 70582); published March 15, 2007

An exact and compact analytical formalism has been developed to calculate the *Q* factor for circular Bragg resonators. The electromagnetic fields, energy, and power flow have been expressed analytically relying on the transfer matrix coefficients. The *Q* factor has been derived for both TM and TE polarizations. The proposed formalism is then compared with two numerical methods. © 2007 Optical Society of America

OCIS codes: 050.2770, 130.3120, 140.3410, 140.4780, 230.1480, 230.5750.

1. INTRODUCTION

Recently, there has been considerable interest in research on optical microresonators, which are key elements for various applications in optical communication systems, such as modulators, filters, lasers, and switches. *Circular* optical resonators were mostly designed as circular distributed Bragg reflectors (DBRs) because of their flexible configuration and optimal light confinement. In fact, circular DBRs offer an additional degree of freedom in the design as they provide a photonic bandgap (PBG) for a sufficient number of grating periods even in the case of low refractive index contrasts. Most of these structures were applied as circular-grating surface-emitting lasers.[1–14] When the circular-grating resonators (CGRs) have shallow trenches, they are called "fingerprint" structures and are mostly modeled using the coupled mode theory (CMT).[15–24] Otherwise, they are called "Bragg leeks" when they have deep trenches and are modeled using the transfer matrix method (TMM).[25–31]

For many of these applications, an optimum design of the CGRs is required to achieve low losses, and thus large quality factors *Q*, so that a better material-photon interaction can be attained within a small modal volume. In fact, the order of magnitude of the *Q* values generally depends on the cavity's degree of symmetry: the highest reported values are therefore observed for whispering-gallery modes in spherical microcavities (10^9–10^{10}).[32] Yet, in the planar case, the best values have been measured at approximately 10^8 for toroid microcavities,[33] and 10^6 for cavities based on defect waveguides in photonic crystal heterostructures.[34] In general, accurate numerical analysis of such high-*Q* microcavities requires a careful handling of the problem (e.g., discretization), which usually involves some iterative refinements of the corresponding model parameters (e.g., mesh). Here, an analytical formalism may provide appropriate measures of the expected resonance and avoid cumbersome numerical calculations. Extensive work to estimate the *Q* factor of highly symmetrical microcavities has been carried out for *spherical*[35–37] and *circular* resonators.[38,39] A general recipe for the optimization of *planar* photonic crystal cavities based on an approximate inverse-problem formula-

tion has been recently proposed by Englund *et al.*[40] It shows how difficult it is to provide an adequate formalism to calculate the Q factor.

This paper focuses on a direct and *analytical* model to calculate the Q factor for the CGR case. Our model does not rely on a complex eigenvalue search, in contrast to, e.g., Ref. 37, where the magnitude of the Q value is inversely proportional to the imaginary part of the eigenfrequency. From a numerical point of view, direct measures of the power leakage are superior to the iterative computation of the aforementioned imaginary eigenvalue contribution, even if both models are analytically represented. In this paper, we designed first-order Bragg CGRs and studied their electromagnetic properties to calculate their Q factor, starting from the most general definition of Q in a microcavity[41]:

$$Q = \omega_{\mathrm{Res}} \frac{\mathcal{W}}{\mathcal{P}}, \tag{1}$$

where $\mathcal{W}$ is the time-averaged energy stored in the cavity and $\mathcal{P}$ the energy leakage out of the cavity. To evaluate $\mathcal{W}$ and $\mathcal{P}$ in our structures, we relied on the general solutions of the electromagnetic field in a cylindrical support and chose to calculate its amplitudes by means of the TMM as this is one of the methods best suited to handle the boundary conditions at the subsequent interfaces in the CGR. The simplest approach is to restrict ourselves to the 2D aspect of the problem and consider the system as being invariant in the z direction.[10,30] Moreover, since the structures are first-order Bragg gratings, the losses are thus restricted to sidewall roughness. This latter could be easily implemented in the TMM model,[42,43] but this is beyond the scope of this paper.

The remainder of the paper is organized as follows. In Section 2 we present the analytical formalism to calculate the Q factor. A practical account of the analytical model is given in Section 3, where we describe various numerical simulations of our CGR based on the finite-element method (FEM). The sensitivity of the results to, e.g., meshing renders the analytical model ideally suited for providing preliminary target values of the resonances investigated that are expected to be attained by the numerical simulation. Section 4 summarizes the present work.

2. MODEL

In this section, we develop an analytical model to calculate the Q factor of our CGRs. We start our analysis with the basic definition of Q given by Eq. (1) and use the TMM model to determine $\mathcal{W}$ and $\mathcal{P}$. We chose the TMM to compute the amplitudes of the electromagnetic fields because, in contrast to the CMT, for example, it permits an exact analysis of high-contrast Bragg structures that cannot be considered as small perturbations. However, the proposed formalism is not limited to this method. Here we will present detailed calculations for TM polarization.

A. Electromagnetic Fields (TM)

Our circular gratings consist of N infinitely extended concentric cylindrical layers of alternating dielectric materials. The layers have outer radii $r_1, \ldots, r_{N-1}$ and refractive indices $n_1, \ldots, n_N$ alternately equal to n_{I} and n_{II}, as illustrated in Fig. 1. We consider the problem two-dimensional and thus invariant in the z direction (i.e., $k_z = 0$). We use cylindrical coordinates (z, r, φ), where r is the distance to the z axis and φ the azimuthal angle. This means that we decompose the planar problem into polar coordinates (r, φ) and a slab (z).

We can then express the electrical and magnetic fields as $\mathbf{E}(r,\varphi)e^{i\omega t}$ and $\mathbf{H}(r,\varphi)e^{i\omega t}$, where ω is the angular frequency of the electromagnetic field, which corresponds to a wave vector in vacuum of $k_0 = \omega/c = 2\pi/\lambda$; c and λ are the light velocity and vacuum wavelength, respectively. Note that $\mathbf{E}(r,\varphi)$ and $\mathbf{H}(r,\varphi)$ are vector fields that are represented by $(\mathcal{E}_z, \mathcal{E}_r, \mathcal{E}_\varphi)$ and $(\mathcal{H}_z, \mathcal{H}_r, \mathcal{H}_\varphi)$, respectively. The $\mathbf{E}$ and $\mathbf{H}$ fields must satisfy the Maxwell equations in each layer j,

$$\nabla \times \mathbf{E} = -\mu_0 i\omega \mathbf{H}, \tag{2}$$

$$\nabla \times \mathbf{H} = \varepsilon_0 n_j^2 i\omega \mathbf{E}, \tag{3}$$

$$\nabla \cdot \mathbf{E} = \nabla \cdot \mathbf{H} = 0, \tag{4}$$

and their tangential components must be continuous at all layer interfaces, μ_0 and ε_0 are the magnetic permeability and the electric permittivity of free space, respectively. For our 2D system, the field solutions can be decomposed into TM and TE polarizations, for which the only nonzero components are $(\mathcal{E}_z, \mathcal{H}_r, \mathcal{H}_\varphi)$ and $(\mathcal{H}_z, \mathcal{E}_r, \mathcal{E}_\varphi)$, respectively. Owing to the cylindrical symmetry of the problem, we expand the fields by means of the first- and second-kind Hankel functions, $H_m = J_m + iN_m$ and $H_m^* = J_m - iN_m$, where m is the azimuthal order, and J_m, N_m are the Bessel and the Neumann functions of order m, respectively. For a given wave vector k, $H_m(kr)$ and $H_m^*(kr)$ are linearly independent and represent outgoing and incoming waves, respectively. The general TM solutions of the Maxwell equations can be expressed for the z component as a linear combination of the independent solutions $H_m(n_j k_0 r)e^{\pm im\varphi}$ and $H_m^*(n_j k_0 r)e^{\pm im\varphi}$ for $m = 0, \ldots, \infty$, in each layer j:

$$\mathcal{E}_z^j(r,\varphi) = \sum_{m=0}^{\infty} [\xi_m^j H_m(n_j k_0 r) + \eta_m^j H_m^*(n_j k_0 r)] e^{\pm im\varphi}. \tag{5}$$

The ± sign in $e^{\pm im\varphi}$ leads to two degenerate modes that give azimuthally counterpropagating modes, which, owing to the rotational symmetry of the problem, have the

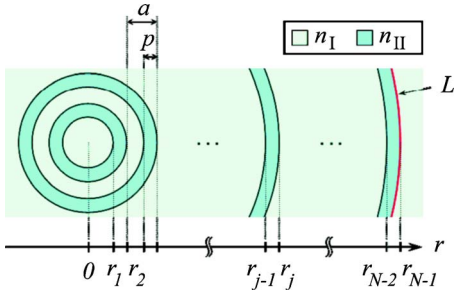

Fig. 1. (Color online) Representation of the structure geometry, with period a, duty cycle d_c defined as p/a, refractive indices n_{I} and n_{II}, inner-cavity radius r_1 and outer radii $r_2, \ldots, r_{N-1}$. L represents the contour of the outermost ring.

same Q. Therefore, we skip the – sign and keep only the + sign, without losing generality. The **E** field is then expressed as $\mathcal{E}_z^j(r,\varphi)=\Sigma_{m=0}^{\infty}\mathcal{E}_z^{j,m}(r)e^{im\varphi}$, where

$$\mathcal{E}_z^{j,m}(r) = \xi_m^j H_m(n_j k_0 r) + \eta_m^j H_m^*(n_j k_0 r). \tag{6}$$

Next, we can extract the transverse **H** field equations using the corresponding Maxwell equation (2), for each layer j:

$$\mathcal{H}_r^j(r,\varphi) = -\frac{1}{\mu_0\omega}\sum_{m=0}^{\infty}[\xi_m^j H_m(n_j k_0 r) + \eta_m^j H_m^*(n_j k_0 r)]me^{im\varphi}, \tag{7}$$

$$= \sum_{m=0}^{\infty}\mathcal{H}_r^{j,m}(r)e^{im\varphi}, \tag{8}$$

$$\mathcal{H}_\varphi^j(r,\varphi) = \frac{n_j}{\mu_0 ic}\sum_{m=0}^{\infty}[\xi_m^j H_m'(n_j k_0 r) + \eta_m^j H_m'^*(n_j k_0 r)]e^{im\varphi}, \tag{9}$$

$$= \sum_{m=0}^{\infty}\mathcal{H}_\varphi^{j,m}(r)e^{im\varphi}, \tag{10}$$

where H_m' is the derivative of H_m with respect to the function argument.

The scope of this work is to calculate the *modal* quality factor Q^m, i.e., the quality factor of each mode m. Therefore, in the remainder of this paper, we will concentrate only on the modal fields $\mathcal{E}_z^{j,m}(r)$, $\mathcal{H}_r^{j,m}(r)$, and $\mathcal{H}_\varphi^{j,m}(r)$, instead of their sums $\mathcal{E}_z^j(r,\varphi)$, $\mathcal{H}_r^j(r,\varphi)$, and $\mathcal{H}_\varphi^j(r,\varphi)$, respectively.

By expressing the continuity of the tangential fields $\mathcal{E}_z$ and $\mathcal{H}_\varphi$ at each layer's interface, it can be shown that the field coefficients in the central cavity are related to those outside the structure by the following transfer matrix relation[10,30]:

$$\begin{pmatrix}\xi_m^N\\ \eta_m^N\end{pmatrix} = \begin{bmatrix}A_m^N & B_m^N\\ B_m^{N*} & A_m^{N*}\end{bmatrix}\begin{pmatrix}\xi_m^1\\ \eta_m^1\end{pmatrix}, \tag{11}$$

where the coefficients A_m^N and B_m^N are functions of n_j, r_j, and k_0. More details about these coefficients are given in Appendix A. The so-called "power-ratio" entity,

$$\mathcal{R}_m = \frac{|\xi_m^1|^2 + |\eta_m^1|^2}{|\xi_m^N|^2 + |\eta_m^N|^2} = \frac{1}{|A_m^N + B_m^N|^2} \tag{12}$$

is plotted in Fig. 2(a) for an example geometry. It was defined by Ochoa *et al.*[30] as a spectral function to probe the cavity resonance, and we already used it in a previous work.[10] Note that we renamed coefficients A_m and B_m from Ref. 10 in Eq. (9) as A_m^N and B_m^N to stress the dependency on the number of layers N. A further discussion on $\mathcal{R}_m$ is provided in Section 3.

B. In-Plane Power Leakage

As we deal with the in-plane problem, we only need to consider the radial power flux $\Re(S_r^{N,m})$, where $\Re(\cdot)$ denotes the real part and $S_r^{N,m}$ the radial component of the Poynting vector $\mathbf{S}=1/2(\mathbf{E}\times\mathbf{H}^*)$, on the contour L of the outermost layer $j=N$ (Fig. 1). The leakage power out of the resonator $\mathcal{P}_m^N$ is given by

$$\mathcal{P}_m^N = \left|\int_L \Re(S_r^{N,m})\mathrm{d}L\right|. \tag{13}$$

For this power leakage-calculation, we define the boundary conditions as

$$\xi_m^1 = 1, \quad \eta_m^N = 0, \tag{14}$$

where we consider that the outgoing wave contribution in the central cavity has unity amplitude ($\xi_m^1=1$) and that no incoming wave impinges from outside ($\eta_m^N=0$).[44] Then Eq. (11) can be rewritten as

$$\begin{pmatrix}\xi_m^N\\ 0\end{pmatrix} = \begin{bmatrix}A_m^N & B_m^N\\ B_m^{N*} & A_m^{N*}\end{bmatrix}\begin{pmatrix}1\\ \eta_m^1\end{pmatrix}, \tag{15}$$

$$\Leftrightarrow \quad \begin{cases}\xi_m^N = (|A_m^N|^2 - |B_m^N|^2)/A_m^{N*}\\ \eta_m^1 = -B_m^{N*}/A_m^{N*}\end{cases}. \tag{16}$$

The radial component $S_r^{N,m}$ is then

$$\begin{aligned}S_r^{N,m} &= -\frac{1}{2}\mathcal{E}_z^{N,m}(r)e^{im\varphi}\mathcal{H}_\varphi^{N,m*}(r)e^{-im\varphi}\\ &= \frac{n_N}{2\mu_0 ic}[\xi_m^N H_m(n_N k_0 r) + \eta_m^N H_m^*(n_N k_0 r)]\\ &\quad\times[\xi_m^{N*} H_m'^*(n_N k_0 r) + \eta_m^{N*} H_m'(n_N k_0 r)]\\ &\overset{\eta_m^N=0}{=} -i\frac{n_N}{2\mu_0 c}|\xi_m^N|^2 H_m(n_N k_0 r)H_m'^*(n_N k_0 r),\end{aligned} \tag{17}$$

and its real part

$$\begin{aligned}\Re(S_r^{N,m}) &= \frac{n_N}{2\mu_0 c}|\xi_m^N|^2\Re(-iH_m H_m'^*)\\ &= \frac{n_N}{2\mu_0 c}|\xi_m^N|^2\Im(H_m H_m'^*)\\ &= \frac{1}{\pi\mu_0\omega r}|\xi_m^N|^2,\end{aligned} \tag{18}$$

where $\omega=k_0 c$. Note that the argument $(n_N k_0 r)$ has been omitted for clarity. Here, the term $\Im(H_m H_m'^*)$ has been simplified as follows

$$\begin{aligned}\Re(-iH_m H_m'^*) &= J_m'(n_N k_0 r)N_m(n_N k_0 r)\\ &\quad - J_m(n_N k_0 r)N_m'(n_N k_0 r)\\ &= -\mathfrak{W}\{J_m(n_N k_0 r), N_m(n_N k_0 r)\}\\ &= -\frac{2}{\pi n_N k_0 r},\end{aligned} \tag{19}$$

where $\Im(\cdot)$ denotes the imaginary part and $\mathfrak{W}\{J_m, N_m\}$ the so-called Wronskian of J_m and N_m.[45] The leakage power is finally expressed by means of μ_0, ω, and the TMM coefficients A_m^N and B_m^N:

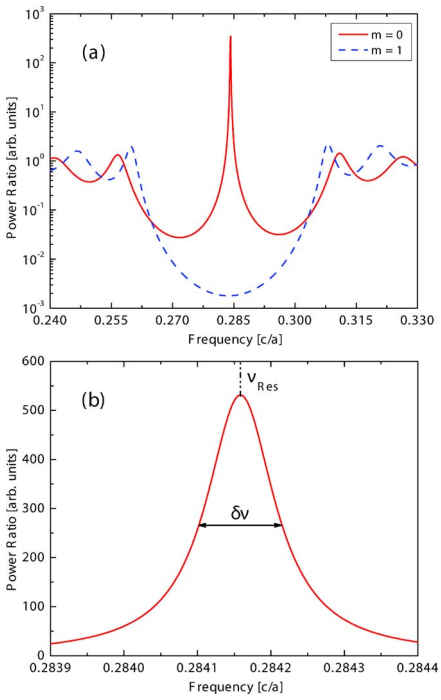

Fig. 2. (Color online) (a) Example of the spectral function $\mathcal{R}_m$ for the two first azimuthal orders $m=0$ and 1, inner-cavity radius $r_1=0.83a$, indices $n_{\mathrm{I}}=1.6$ and $n_{\mathrm{II}}=1.96$, number of layers $N=32$, and duty cycle $d_c=0.45$. (b) Zoom of the resonance peak and the FWHM of the linewidth $\delta\nu$ at the resonance frequency ν_{Res}.

$$\mathcal{P}_m^N = \int_0^{2\pi} \frac{1}{\pi\mu_0\omega r}|\xi_m^N|^2 r\mathrm{d}\varphi = \frac{2}{\mu_0\omega}|\xi_m^N|^2 = \frac{2}{\mu_0\omega}\frac{(|A_m^N|^2-|B_m^N|^2)^2}{|A_m^N|^2}. \tag{20}$$

C. Energy

The time-averaged energy density $w^{j,m}$ of the mth mode, stored inside a layer j, can be calculated by using only the electric field and the electric permittivity of the material $\varepsilon_j=\varepsilon_0 n_j^2$ (Refs. 46 and 47):

$$w^{j,m} = \tfrac{1}{2}\varepsilon_j|\mathcal{E}_z^{j,m}(r)|^2. \tag{21}$$

Here, we assume that the energy density in the cavity relies upon two equal parts, namely, the individual contributions from the electric field and the magnetic field. For leaky cavities, the magnitudes of the two fields are governed by the corresponding boundary conditions at the cavity's outermost interface. Hence there is a small imbalance between these two contributions,[32] which vanishes for high Q factors, with the result that our assumption remains valid.

Furthermore, we assume a stationary case, i.e., a standing wave for which the inward and outward propagating wave contributions are equal. Indeed, in the case of a leaky cavity, for which we calculated the power leakage in Subsection 2.B, this is not strictly the case. Yet again, for low leakage, this imbalance gives a negligible contribution for the stored energy. Therefore, when estimating the energy in the microcavity, we can use the stationary case condition:

$$\xi_m^1 = \eta_m^1 = 1. \tag{22}$$

Note that without the assumption $\xi_m^1=\eta_m^1$, the field would diverge at the origin, owing to the presence of the Neumann function in H_m, and that choosing unity results in a normalization of the cavity energy at resonance. So, if we rewrite Eq. (11) for any layer j, we obtain

$$\begin{pmatrix}\xi_m^j\\ \eta_m^j\end{pmatrix} = \begin{bmatrix}A_m^j & B_m^j\\ B_m^{j*} & A_m^{j*}\end{bmatrix}\begin{pmatrix}1\\1\end{pmatrix}, \tag{23}$$

$$\Leftrightarrow \quad \begin{cases}\xi_m^j = A_m^j + B_m^j\\ \eta_m^j = B_m^{j*} + A_m^{j*} = \xi_m^{j*}.\end{cases} \tag{24}$$

This allows us to rewrite Eq. (6) as $\mathcal{E}_z^{j,m}(r)=2\Re\{(A_m^j+B_m^j)H_m(n_jk_0r)\}$ for the electric field. Under the condition (22), $\mathcal{E}_z^{j,m}(r)$ is real for every layer j and its norm can be written as

$$|\mathcal{E}_z^{j,m}(r)|^2 = [\mathcal{E}_z^{j,m}(r)]^2 = 4[\Re^2(A_m^j+B_m^j)J_m^2(n_jk_0r) + \Im^2(A_m^j+B_m^j)N_m^2(n_jk_0r) - 2\Re(A_m^j+B_m^j) \times \Im(A_m^j+B_m^j)J_m(n_jk_0r)N_m(n_jk_0r)]. \tag{25}$$

Figure 3 shows the corresponding $\mathcal{E}_z$ for the same example geometry as used in Fig. 2 ($m=0$ and $N=32$). The total time-averaged energy $\mathcal{W}^{j,m}$ of the mth mode, stored in each layer j, is then the integral of $w^{j,m}$ over the layer's area $\mathcal{A}_j$:

$$\mathcal{W}^{j,m} = \int_{\mathcal{A}_j} w^{j,m}\mathrm{d}\mathcal{A}_j = \frac{1}{2}\int_\varphi\int_r \varepsilon_j|\mathcal{E}_z^{j,m}(r)|^2 r\mathrm{d}r\mathrm{d}\varphi = \pi\varepsilon_0 n_j^2\int_{r_{j-1}}^{r_j}\mathcal{E}_z^{j,m}(r)^2 r\mathrm{d}r. \tag{26}$$

The total modal energy in the microcavity is then expressed by $\mathcal{W}^m=\Sigma_{j=1}^N\mathcal{W}^{j,m}$:

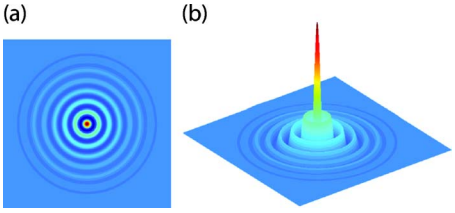

Fig. 3. (Color online) (a) Two-dimensional and (b) 3D graphs of the $\mathcal{E}_z^{j,0}$ field in the case of $(n_{\mathrm{I}},n_{\mathrm{II}})=(1.6,1.96)$, $N=32$ layers, cavity radius of $r_1=0.83a$, with a being the lattice constant and $d_c=0.45$, for the monopole mode ($m=0$) at resonance.

$$\mathcal{W}^m = 4\pi\varepsilon_0 \sum_{j=1}^{N} n_j^2 \Bigg[\underbrace{\Re^2(A_m^j + B_m^j)}_{\gamma_J} \underbrace{\int_{r_{i-1}}^{r_j} J_m^2(n_j k_0 r) r \mathrm{d}r}_{W_J^m} + \underbrace{\Im^2(A_m^j + B_m^j)}_{\gamma_N} \underbrace{\int_{r_{j-1}}^{r_j} N_m^2(n_j k_0 r) r \mathrm{d}r}_{W_N^m} - \underbrace{2\Re(A_m^j + B_m^j)\Im(A_m^j + B_m^j)}_{\gamma_{JN}} \times \underbrace{\int_{r_{j-1}}^{r_j} J_m(n_j k_0 r) N_m(n_j k_0 r) r \mathrm{d}r}_{W_{JN}^m} \Bigg], \tag{27}$$

which gives a compact and simple formula for the modal energy in the overall cavity:

$$\mathcal{W}^m = 4\pi\varepsilon_0 \sum_{j=1}^{N} n_j^2 W^{j,m}, \tag{28}$$

where

$$W^{j,m} = \gamma_J W_J^m + \gamma_N W_N^m + \gamma_{JN} W_{JN}^m. \tag{29}$$

The integrals W_J^m, W_N^m, and W_{JN}^m are known,[48–50] and their analytical solutions are presented in more detail in Appendix B.

D. Q Factor

Using Eqs. (1), (20), and (28), we can finally express the Q factor, Q_{TM}^m, of the mth mode for the TM polarization at ω_{Res} by

$$Q_{\mathrm{TM}}^m = \omega_{\mathrm{Res}} \frac{\mathcal{W}^m}{\mathcal{P}_m^N} = 2\pi k_{\mathrm{Res}}^2 \frac{|A_m^N|^2}{(|A_m^N|^2 - |B_m^N|^2)^2} \sum_{j=1}^{N} n_j^2 W^{j,m}, \tag{30}$$

where $k_{\mathrm{Res}}^2 = \omega_{\mathrm{Res}}^2 \varepsilon_0 \mu_0$. Table 1 summarizes the results of this analysis for both TM and TE polarizations. See Appendix C for more details about the TE formulas. This final result can be used for any CGR and is easy to implement. The numerical implementation is shown in the next section.

3. RESULTS AND DISCUSSION

As a case study, the evaluation of the analytical model is performed for a CGR with the following parameters: (i) The indices, $n_{\mathrm{I}} = 1.6$ and $n_{\mathrm{II}} = 1.96$, are chosen according to a realistic material system. (ii) The lattice constant or grating period is set to a, to which all the other parameters are normalized, namely, the normalized frequency $\nu[c/a]$ and the cavity radius $r_1[a]$. (iii) The duty cycle, $d_c = p/a = 0.45$ (Fig. 1), was optimized to obtain the largest PBG for this configuration. (iv) The number of layers $N = 32$, which is a sufficient and reasonable number to achieve the desired reflecting properties.

Table 1. Recapitulation of Energy, Power, and Q Factor[a]

	TM	Equation	TE	Equation
$\mathcal{P}_N^m$	$\frac{2}{\mu_0\omega}\chi_m^2$	(20)	$\frac{2}{\varepsilon_0 n_N^2 \omega}\chi_m^2$	(C6)
$\mathcal{W}^m$	$4\pi\varepsilon_0 \sum_{j=1}^{N} n_j^2 W^{j,m}$	(28)	$4\pi\mu_0 \sum_{j=1}^{N} W^{j,m}$	(C7)
Q^m	$2\pi k_{\mathrm{Res}}^2 \chi_m^{-2} \sum_{j=1}^{N} n_j^2 W^{j,m}$	(30)	$2\pi n_N^2 k_{\mathrm{Res}}^2 \chi_m^{-2} \sum_{j=1}^{N} W^{j,m}$	(C9)

[a]Recapitulation of energy $\mathcal{W}^m$, power $\mathcal{P}_N^m$, and Q Factor Q^m for both TM and TE polarization by means of the transfer-matrix coefficients A_m^N and B_m^N. The new variable $\chi_m^2 = (|A_m^N|^2 - |B_m^N|^2)/|A_m^N|^2$ is defined here for convenience.

One of the design strategies is to retrieve the optimum cavity radius that yields the highest Q for each mode m. For that purpose, we scanned over the inner-cavity radii for the two first modes of interest, namely, $m = 0$ (monopole) and $m = 1$ (dipole). Maximum Q values are expected for an inner-cavity radius for which the resonance frequency lies in the center of the PBG, where the reflection of the gratings reaches its maximum and thus the cavity loss its minimum. The resonances are first found using the power-ratio function $\mathcal{R}_m$ [Eq. (12)]. For illustration, Fig. 4(a) shows the power-ratio plots of the dipole mode ($m = 1$) for three different cavity radii $r_1 = 1.0a$, $1.35a$, and $1.8a$. Figure 4(b) shows the behavior of the resonances versus the cavity radii over the entire PBG range, i.e., between $0.26c/a$ and $0.31c/a$. We denote by R_0 the inner cavity radius for the monopole $m = 0$ and by R_1 that for the dipole $m = 1$. The radii for which the resonances are located in the center of the PBG are $R_0 = 0.83a$ and $R_1 = 1.35a$.

First, the corresponding Q values are analytically calculated for all these resonances as explained in Section 2, and the results are depicted in Fig. 5(a) for $m = 0$ (solid circles) and for $m = 1$ (solid triangles). The scan over the cavity radii has a peak shape with maxima at $R_0 = 0.83a$ and $R_1 = 1.35a$. These data underpin the fact that optimum Q values stem from cavity resonances located in the center of the PBG.

As an intuitive and straightforward approach, one can mostly rely on spectral functions, such as Ochoa's power-ratio $\mathcal{R}_m$ [Eq. (12)], to extract the FWHM definition of the Q factor [Fig. 2(b)]:

$$Q = \frac{\nu_{\mathrm{Res}}}{\delta\nu}, \tag{31}$$

where ν_{Res} is the resonance frequency and $\delta\nu$ the linewidth. For comparison, the results for both the monopole (open circles) and dipole modes (open triangles) have been added to Fig. 5(a). The new graphs exhibit a similar peak shape as that of the analytical Q graphs. We can see that

in both cases the FWHM estimation of the Q value is higher around the center of the PBG than the exact analytical one. The difference percentage $\Delta=(Q_{\mathrm{FWHM}}-Q_{\mathrm{Analytic}})/Q_{\mathrm{Analytic}}$ is in the range of $\sim[-40\%,20\%]$ for $m=0$ and $\sim[-40\%,60\%]$ for $m=1$ [Fig. 5(b)]. This result is interesting, but very difficult to interpret because Ochoa's $\mathcal{R}_m$ function does not represent a clearly defined fundamental physical entity. This function gives the spectral information of the structure, i.e., the resonance frequencies, but does not seem to reflect the proper Q information. Even though a more pertinent alternative to $\mathcal{R}_m$ would be to probe the spectral response of the cavity energy $\mathcal{W}^m$, this would still involve a conceptual pitfall, which is discussed in Ref. 51. However, for most practical cases, such spectral responses may still serve as a good qualitative figure of merit when no exact analytical result is provided.

To obtain more information on the behavior of the Q calculations versus the number of layers in the structures, we fix the inner cavity radii to $R_0=0.83a$ and $R_1=1.35a$, for the optimum Q values i.e., for center-PBG resonances, and to $R_0=1.2a$ and $R_1=1.8a$ for a worst-case scenario, i.e., for edge-PBG resonances. Then, we scan over the number of layers, i.e., $N=32$, 40, 48, and 64, and display both the analytical and the FWHM results in Figs. 6(a) for $m=0$ and in 6(b) for $m=1$. The two modes exhibit a similar behavior: there is an exponential increase of the Q factor with increasing number of layers as

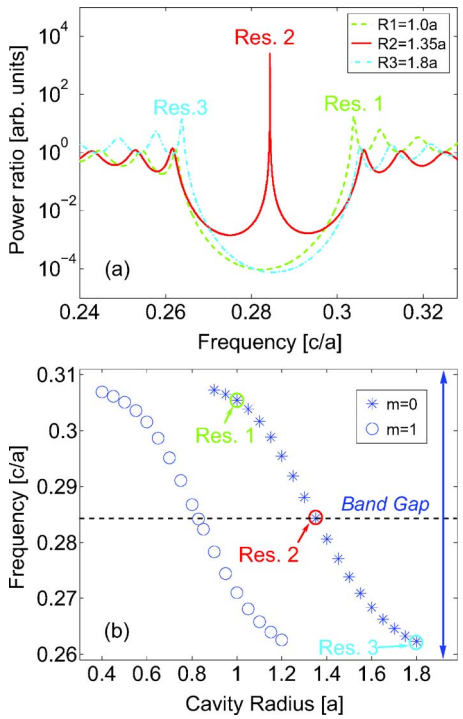

Fig. 4. (Color online) Cavity design: (a) typical power-ratio plot for a dipole mode $m=1$ at three different inner-cavity radii, i.e., $r_1=1.0a$, $1.35a$, and $1.8a$. Resonances Res. 1, Res. 2, and Res. 3 are located at the lower band edge, at the middle of the PBG, and at the higher band edge, respectively. (b) Scan over the cavity radii of the resonances for the azimuthal orders $m=0$ (monopole) and $m=1$ (dipole). Maximum Q is expected at radii where the resonance is in the middle of the PBG, which, in our case, are $R_0=0.83a$ and $R_1=1.35a$. For clarity, Res. 1, Res. 2, and Res. 3 of (a) are also indicated here.

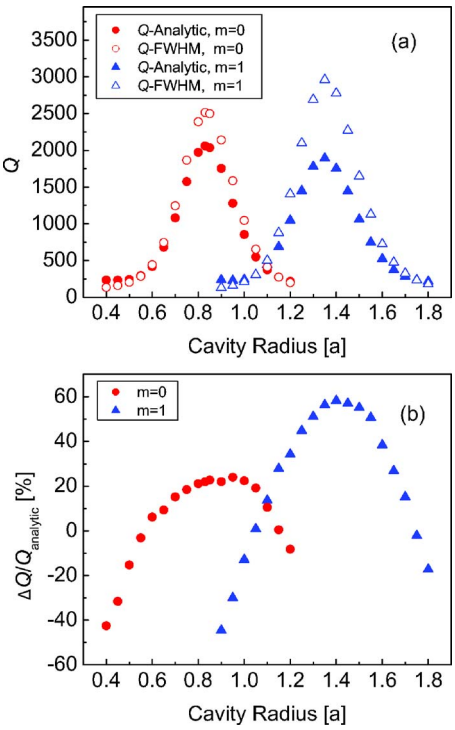

Fig. 5. (Color online) Q-factor calculation with both methods: analytically and with FWHM (power ratio) for $N=32$ layers, $m=0$ (circles), and $m=1$ (triangles). (a) Scan over the cavity radii: maximum Q value is the one located in the center of the PBG as illustrated in Fig. 4, i.e., $R_0=0.83a$ for $m=0$ and $R_1=1.35a$ for $m=1$. (b) Difference percentage $\Delta=(Q_{\mathrm{FWHM}}-Q_{\mathrm{Analytic}})/Q_{\mathrm{Analytic}}$ is plotted for both m orders.

theoretically expected from the evanescent mode tails in the grating structure. The difference between the two methods is constant for the optimum case (center of PBG), i.e., $\Delta\sim 20\%$ for $R_0=0.83a$ and $\sim 57\%$ for $R_1=1.35a$. Note that the discrepancy is larger for the dipole case. However, it tends to become more negligible for the worst case (edge of PBG) the more layers there are, i.e., for $R_0=1.2a$ it decreases from -11% to -5%, and for $R_1=1.8a$ from -15% to -9%, when N increases from 32 to 64. Therefore, the FWHM estimation of the Q factor from the $\mathcal{R}_m$ spectral function could be used, with care, for low-mode orders and band edge cases.

Finally, to underpin the usefulness of our analytical approach, we performed a complementary numerical cross-check by using a FEM tool, namely, FEMLAB,[52] and analyzed the same example geometry. For this comparison, we chose the optimum geometry for the dipole's case, i.e., $R_1=1.35a$. The simulation was done by exciting the cavity with a double-circle push–pull excitation instead of a double-point one because the latter is not possible in FEMLAB (Fig. 7). The results are also depicted in Fig. 6 as black diamonds and error bars. The Q values obtained are in the same order of magnitude as those of the two other methods but do not seem to vary in the same parallel way. Nevertheless, one has to be careful with the interpretation of these simulations because many numerical parameters, e.g., the resolution of the meshing grid and the excitations' locations, may play a role and change the resulting Q values. In fact, we varied the distance δ between the excitations for three cases: $\delta=80$ nm (upper

error bars), $\delta=200$ nm (black diamonds), and $\delta=320$ nm (lower error bars). It is clear from Fig. 6 that there is a deviation between the three cases, which increases with the number of layers, i.e., with increasing Q values. Yet, the most appropriate case is the $\delta=320$ nm one, where the two circle excitations are located exactly on the extrema of the dipole mode, as illustrated in Fig. 7. This shows how difficult it is to choose the appropriate parameters in a numerical method: because of the latter's sensitivity, the analytical model is thus shown to be best suited for providing target values for Q independently of any parameter. Nonetheless, we can rely on FEMLAB simulations for the Q estimation, at least for a reasonable number of layers, which is necessary especially when dealing with more complicated device designs.

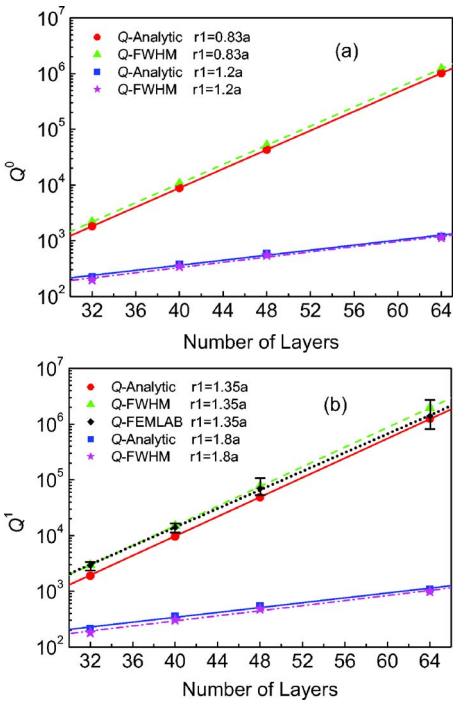

Fig. 6. (Color online) Comparison of the Q values obtained with the different methods for $N=32$, 40, 48, and 64. (a) Monopole ($m=0$): example of the central-PBG cavity radius, $R_0=0.83a$, and an edge-PBG one, $R_0=1.2a$. Ratio between the FWHM values and the analytical ones is ~20% for $R_0=0.83a$ and −8% (mean value) for $R_0=1.2a$. (b) Dipole ($m=1$): same as (a) but for two cavity radii $R_1=1.35a$ and $R_1=1.8a$. Ratio between the FWHM values and the analytical ones is ~57% for $R_1=1.35a$ and −13% (mean value) for $R_1=1.8a$. Here, we also added some FEMLAB calculations of the Q factor (black diamonds and error bars), only for the $R_1=1.35a$ case.

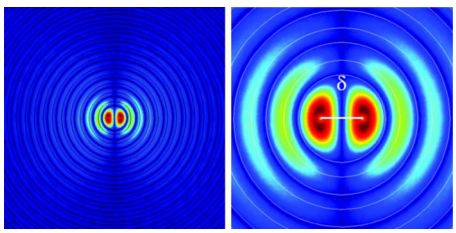

Fig. 7. (Color online) $|\mathcal{E}_z|^2$ field calculated with FEMLAB for the dipole mode ($R_1=1.35a$, $N=32$ layers, $\lambda=850$ nm, $a=240$ nm). Distance between the two excitations, $\delta=320$ nm, is illustrated in the close-up of the cavity (right). The two circle excitations have a radius of 10 nm.

4. CONCLUSION

We developed an exact *analytical* formalism to calculate the Q factor for planar circular Bragg microcavities using the TMM for both TM and TE polarizations. The need for an analytical procedure is underpinned by the fact that most alternative methods encounter difficulties when tracking down accurate quality factors in the high-Q regime.

Here, we argued that the commonly performed FWHM estimation of the cavity's spectral response essentially depends on the technical setting necessary to access the corresponding field quantity. Hence the spectrally determined Q factors become context dependent.

Another complication arises when relying on domain methods, such as the FEM, for the numerical simulation of resonant cavities. In fact, by slightly altering the position of the cavity excitation, for example, we were able to infer that only a well-adapted domain discretization (meshing) can yield reliable Q values.

Yet, the analytical method presented is extremely fast and best suited to provide accurate measures for all kinds of circular cavities. The latter becomes necessary when optimizing circular-grating configurations to be used in combination with numerical tools such as FEMLAB, for fast all-optical switching applications, for example.[53]

APPENDIX A: TRANSFER MATRLX METHOD COEFFICIENTS

Expressing the boundary conditions for TM polarization at the different layer interfaces (for $j=1,\ldots,N-1$) by

$$\mathcal{E}_z^j(r_j,\varphi)=\mathcal{E}_z^{j+1}(r_j,\varphi), \tag{A1}$$

$$\mathcal{H}_\varphi^j(r_j,\varphi)=\mathcal{H}_\varphi^{j+1}(r_j,\varphi), \tag{A2}$$

we obtain the transfer matrix between two adjacent layers for different azimuthal numbers m:

$$\begin{pmatrix}\xi_m^{j+1}\\ \eta_m^{j+1}\end{pmatrix}=\begin{bmatrix}\alpha_m^j & b_m^j\\ b_m^{j*} & \alpha_m^{j*}\end{bmatrix}\begin{pmatrix}\xi_m^j\\ \eta_m^j\end{pmatrix}, \tag{A3}$$

where

$$\alpha_m^j=\frac{1}{D_m^j}\left[H_m(n_jr_jk_0)H_m'^*(n_{j+1}r_jk_0)-\frac{n_{j+1}}{n_j}H_m^*(n_{j+1}r_jk_0)H_m'(n_jr_jk_0)\right], \tag{A4}$$

$$b_m^j=\frac{1}{D_m^j}\left[H_m^*(n_jr_jk_0)H_m'^*(n_{j+1}r_jk_0)-\frac{n_{j+1}}{n_j}H_m^*(n_{j+1}r_jk_0)H_m'^*(n_jr_jk_0)\right], \tag{A5}$$

$$D_m^j=H_m(n_{j+1}r_jk_0)H_m'^*(n_{j+1}r_jk_0)-H_m^*(n_{j+1}r_jk_0)H_m'(n_{j+1}r_jk_0). \tag{A6}$$

For TE polarization, we only have to replace the ratio n_j/n_{j+1} by n_{j+1}/n_j in Eqs. (A4) and (A5). If we subse-

quently multiply the transfer matrices (A3) for each layer, we obtain an overall transfer matrix (A8) relating the inner cavity to the outermost ring of the structure: for $j=1,\ldots,N-1$,

$$\begin{pmatrix} \xi_m^N \\ \eta_m^N \end{pmatrix} = \begin{bmatrix} A_m^N & B_m^N \\ B_m^{N*} & A_m^{N*} \end{bmatrix} \begin{pmatrix} \xi_m^1 \\ \eta_m^1 \end{pmatrix}, \tag{A7}$$

where the transfer matrix is

$$\begin{bmatrix} A_m^N & B_m^N \\ B_m^{N*} & A_m^{N*} \end{bmatrix} = \begin{bmatrix} a_m^{N-1} & b_m^{N-1} \\ b_m^{N-1*} & a_m^{N-1*} \end{bmatrix} \cdots \begin{bmatrix} a_m^1 & b_m^1 \\ b_m^{1*} & a_m^{1*} \end{bmatrix}. \tag{A8}$$

By definition, the first coefficients are $A_m^1=1$ and $B_m^1=0$.

APPENDIX B: BESSEL AND NEUMANN FINITE INTEGRALS

As discussed in Subsection 2.C, the total modal energy is expressed by the simple formula $\mathcal{W}^m=4\pi\epsilon_0\Sigma_{j=1}^N n_j^2 W^{j,m}$, with $W^{j,m}=\gamma_J W_J^m+\gamma_N W_N^m+\gamma_{JN} W_{JN}^m$ [Eq. (29)]. The constants γ_J, γ_N, and γ_{JN} are already defined in Eq. (27). The integrals W_J^m, W_N^m, and W_{JN}^m can be solved analytically[48–50] and the solutions are given by

$$W_J^m = \frac{1}{2} r^2 [J_m(n_j k_0 r)^2 - J_{m-1}(n_j k_0 r) J_{m+1}(n_j k_0 r)] \Big|_{r_{j-1}}^{r_j}, \tag{B1}$$

$$W_N^m = \frac{1}{2} r^2 [N_m(n_j k_0 r)^2 - N_{m-1}(n_j k_0 r) N_{m+1}(n_j k_0 r)] \Big|_{r_{j-1}}^{r_j}, \tag{B2}$$

$$W_{JN}^m = \frac{1}{4} r^2 [J_m(n_j k_0 r) N_m(n_j k_0 r) - 2J_{m+1}(n_j k_0 r) N_{m-1}(n_j k_0 r) - 2J_{m-1}(n_j k_0 r) N_{m+1}(n_j k_0 r)] \Big|_{r_{j-1}}^{r_j}. \tag{B3}$$

Note that we calculate the modal energy for the stationary case, i.e., under condition (22). Thus for the special case of the first layer, i.e., the inner cavity, the first term in Eq. (27) nonzero and reduces to

$$\mathcal{W}^{1,m} = 4\pi\varepsilon_0 n_1^2 \underbrace{\int_0^{r_1} J_m^2(n_1 k_0 r) r \mathrm{d}r}_{W^{1,m}}, \tag{B4}$$

with the analytical solution of the integral $W^{1,m}$:

$$W^{1,m} = 2^{-2-2m}\sqrt{\pi}\frac{r_1^{m+1}}{(n_1 k_0)^{4m}}\frac{\Gamma(m+3/2)}{\Gamma(m+2)\Gamma(m+1)}\mathfrak{S}_m(2n_1 k_0 r_1), \tag{B5}$$

where $\mathfrak{S}_m$ is the Struve function of order m and Γ is the gamma function.[45,50]

APPENDIX C: TE POLARIZATION

TE-polarized electromagnetic fields. The general TE solutions of the Maxwell equations are expressed by

$$\mathcal{H}_z^j(r,\varphi) = \sum_{m=0}^{\infty} [\xi_m^j H_m(n_j k_0 r) + \eta_m^j H_m^*(n_j k_0 r)] e^{im\varphi} = \sum_{m=0}^{\infty} \mathcal{H}_z^{j,m}(r) e^{im\varphi}, \tag{C1}$$

$$\mathcal{E}_r^j(r,\varphi) = \frac{1}{\varepsilon_0 n_j^2 \omega}\sum_{m=0}^{\infty} [\xi_m^j H_m(n_j k_0 r) + \eta_m^j H_m^*(n_j k_0 r)] m e^{im\varphi} = \sum_{m=0}^{\infty} \mathcal{E}_r^{j,m}(r) e^{im\varphi}, \tag{C2}$$

$$\mathcal{E}_r^j(r,\varphi) = \frac{1}{\varepsilon_0 n_j c}\sum_{m=0}^{\infty} [\xi_m^j H_m'(n_j k_0 r) + \eta_m^j H_m'^*(n_j k_0 r)] e^{im\varphi} = \sum_{m=0}^{\infty} \mathcal{E}_\varphi^{j,m}(r) e^{im\varphi}. \tag{C3}$$

Power leakage. The radial component of the Poynting vector $S_r^{N,m}$, its real part, and the power leakage are, respectively,

$$S_r^{N,m} = \frac{1}{2}\mathcal{H}_z^{N,m*}(n_N k_0 r)\mathcal{E}_\varphi^{N,m}(n_N k_0 r) = \frac{i}{2\varepsilon_0 n_N c}|\xi_m^N|^2 H_m^* H_m', \tag{C4}$$

$$\Re(S_\tau^{N,m}) = \frac{1}{2\varepsilon_0 n_N c}|\xi_m^N|^2 \Im(H_m H_m'^*) = \frac{1}{\pi\varepsilon_0 n_N^2 \omega r}|\xi_m^N|^2, \tag{C5}$$

$$\mathcal{P}_m^N = \frac{2}{\varepsilon_0 n_N^2 \omega}|\xi_m^N|^2 = \frac{2}{\varepsilon_0 n_N^2 \omega}\frac{(|A_m^N|^2 - |B_m^N|^2)^2}{|A_m^N|^2}. \tag{C6}$$

Energy. Similarly to the TM case, the total time-averaged energy $\mathcal{W}^m$ is expressed as

$$\mathcal{W}^m = \frac{1}{2}\int_{\mathcal{A}} \mu_0 |\mathcal{H}_z^{j,m}(r)|^2 \mathrm{d}\mathcal{A}$$

$$= \pi\mu_0 \int_r \mathcal{H}_z^{j,m}(r)^2 r\mathrm{d}r = 4\pi\mu_0 \sum_{j=1}^{N} W^{j,m}, \qquad \text{(C7)}$$

where $W^{j,m}$ is the same as that given in Eq. (29). The energy in the cavity is reduced to

$$\mathcal{W}^{1,m} = 4\pi\mu_0 \underbrace{\int_0^{r_1} J_m^2(n_j k_0 r) r\mathrm{d}r}_{W^{1,m}}, \qquad \text{(C8)}$$

where $W^{1,m}$ is given by Eq. (B5).

Q factor. Similarly to Eq. (30), the Q factor at $\omega_{\mathrm{Res}} = k_{\mathrm{Res}}\, c$ is given by

$$Q_{\mathrm{TE}}^m = 2\pi n_N^2 k_{\mathrm{Res}}^2 \frac{|A_m^N|^2}{(|A_m^N|^2 - |B_m^N|^2)^2} \sum_{j=1}^{N} W^{j,m}. \qquad \text{(C9)}$$

ACKNOWLEDGMENTS

The authors thank Roman Kappeler and Daniel Lenz for fruitful discussions. This work has been supported by the Swiss National Centre of Competence in Research (NCCR) in Quantum Photonics. The ETH Zurich Innovation Initiative (INIT) for the supportive framework also deserves special mention.

A. Jebali's e-mail address is jebali@photonics.ee.ethz.ch.

REFERENCES AND NOTES

1. D. Labilloy, H. Benisty, C. Weisbuch, T. F. Krauss, C. J. M. Smith, R. Houdré, and U. Oesterle, "High-finesse disk microcavity based on a circular Bragg reflector," Appl. Phys. Lett. **73**, 1314–1316 (1998).
2. C. Wu, M. Svilans, M. Fallahi, T. Makino, J. Glinski, C. Maritan, and C. Blaauw, "Optically pumped surface-emitting DFB GalnAsP/InP lasers with circular grating," Electron. Lett. **27**, 1819–1821 (1991).
3. T. Erdogan, O. King, G. W. Wicks, D. G. Hall, E. H. Anderson, and M. J. Rooks, "Circularly symmetric operation of a concentric-circle-grating, surface-emitting, AlGaAs/GaAs quantum-well semiconductor laser," Appl. Phys. Lett. **60**, 1921–1923 (1992).
4. C. Olson, P. L. Greene, G. W. Wicks, D. G. Hall, and S. Rishton, "High-order azimuthal spatial modes of concentric-circle-grating surface-emitting semiconductor lasers," Appl. Phys. Lett. **72**, 1284–1286 (1998).
5. A. Shaw, B. Roycroft, J. Hegarty, D. Labilloy, H. Benisty, C. Weisbuch, T. F. Krauss, C. J. M. Smith, R. Stanley, R. Houdre, and U. Oesterle, "Lasing properties of disk microcavity based on a circular Bragg reflector," Appl. Phys. Lett. **75**, 3051–3053 (1999).
6. M. Fallahi, F. Chatenoud, M. Dion, I. Templeton, R. Barber, and J. Thompson, "Circular-grating surface-emitting distributed Bragg reflector lasers on an InGaAs-GaAs structure for 0.98-μm applications," IEEE J. Sel. Top. Quantum Electron. **1**, 382–386 (1995).
7. A. M. Shams-Zadeh-Amiri, X. Li, and W.-P. Huang, "Hankel transform-domain analysis of scattered fields in multilayer planar waveguides and lasers with circular gratings," IEEE J. Quantum Electron. **39**, 1086–1098 (2003).
8. C. Bauer, H. Giessen, B. Schnabel, E. B. Kley, C. Schmitt, U. Scherf, and R. F. Mahrt, "A surface-emitting circular grating polymer laser," Adv. Mater. (Weinheim, Ger.) **13**, 1161–1164 (2001).
9. N. Moll, C. Bauer, H. Giessen, B. Schnabel, E. B. Kley, U. Scherf, and R. F. Mahrt, "Evidence for bandedge lasing in a two-dimensional photonic bandgap polymer laser," Appl. Phys. Lett. **80**, 734–736 (2002).
10. A. Jebali, R. F. Mahrt, N. Moll, D. Erni, C. Bauer, E. B. Kley, G. L. Bona, and W. Bächtold, "Lasing in organic circular grating structures," J. Appl. Phys. **96**, 3043–3049 (2004).
11. G. F. Barlow, A. Shore, G. A. Turnbu, and I. D. W. Samuel, "Design and analysis of a low-threshold polymer circular-grating distributed-feedback laser," J. Opt. Soc. Am. B **21**, 2142–2150 (2004).
12. G. A. Turnbull, A. Carleton, G. F. Barlow, A. Tahraoui, T. F. Krauss, A. Shore, and I. D. W. Samuel, "Design and analysis of a low-threshold polymer circular-grating distributed- feedback laser," J. Appl. Phys. **98**, 023105 (2005).
13. J. Scheuer, W. M. J. Green, G. A. DeRose, and A. Yariv, "InGaAsP annular Bragg lasers: theory, applications, and modal properties," IEEE J. Sel. Top. Quantum Electron. **11**, 476–484(2005).
14. J. Scheuer, W. M. J. Green, G. A. DeRose, and A. Yariv, "Lasing from a circular Bragg nanocavity with an ultrasmall modal volume," Appl. Phys. Lett. **86**, 251101 (2005).
15. T. Erdogan and D. G. Hall, "Circularly symmetric distributed feedback semiconductor laser: An analysis," J. Appl. Phys. **68**, 1435–1444 (1990).
16. T. Erdogan and D. G. Hall, "Circularly symmetric distributed feedback laser: coupled mode treatment of TE vector fields," IEEE J. Quantum Electron. **28**, 612–623 (1992).
17. C. Wu, T. Makino, J. Glinski, R. Maciejko, and S. I. Najafi, "Self-consistent coupled-wave theory for circular gratings on planar dielectric waveguides," J. Lightwave Technol. **9**, 1264–1277 (1991).
18. C. Wu, T. Makino, R. Maciejko, S. I. Najafi, and M. Svilans, "Simplified coupled-wave equations for cylindrical waves in circular grating planar waveguides," J. Lightwave Technol. **10**, 1575–1589 (1992).
19. X. M. Gong, A. K. Chan, and H. F. Taylor, "Lateral mode discrimination in surface emitting DBR lasers with cylindrical symmetry," IEEE J. Quantum Electron. **30**, 1212–1218 (1994).
20. M. Toda, "Single-mode behavior of a circular grating for potential disk-shaped DFB lasers," IEEE J. Quantum Electron. **26**, 473–481 (1990).
21. A. Yariv, ed. *Optical Electronics in Modern Communications* (Oxford U. Press, 1997).
22. P. L. Greene and D. G. Hall, "Effects on radiation on circular-grating DFB lasers—Part I: coupled-mode equations," IEEE J. Quantum Electron. **37**, 353–364 (2001).
23. P. L. Greene and D. G. Hall, "Effects on radiation on circular-grating DFB lasers—Part II: device and pump-beam parameters," IEEE J. Quantum Electron. **37**, 365–371 (2001).
24. J. Scheuer and A. Yariv, "Coupled-waves approach to the design and analysis of Bragg and photonic crystal annular resonators," IEEE J. Quantum Electron. **39**, 1555–1561 (2003).
25. P. Ye, A. Yariv, and E. Marom, "Theory of Bragg fiber," J. Opt. Soc. Am. **68**, 1196–1201 (1978).
26. T. Kawanishi and M. Izutsu, "Coaxial periodic optical waveguide," Opt. Express **7**, 10–22 (2000).
27. E. X. Ping, "Transmission of electromagnetic waves in planar, cylindrical, and spherical dielectric layer systems and their applications," J. Appl. Phys. **76**, 7188–7194 (1994).
28. M. A. Kaliteevski, R. A. Abram, V. V. Nikolaev, and G. S. Sokolovski, "Bragg reflectors for cylindrical waves," J. Mod. Opt. **46**, 875–890 (1999).
29. C. C. Wang and Z. Ye, "Spontaneous emission in cylindrical

periodically-layered structures," Phys. Status Solidi A **174**, 527–540 (1999).
30. D. Ochoa, R. Houdré, M. Ilegems, H. Benisty, T. F. Krauss, and C. J. M. Smith, "Diffraction of cylindrical Bragg reflectors surrounding an in-plane semiconductor microcavity," Phys. Rev. B **61**, 4806–4812 (2000).
31. J. Scheuer and A. Yariv, "Annular Bragg defect mode resonators," J. Opt. Soc. Am. B **20**, 2285–2291 (2003).
32. R. K. Chang and A. J. Campillo, *Optical Processes in Microcavities* (World Scientific, 1996), pp. 27–34.
33. D. K. Armani, T. J. Kippenberg, S. M. Spillane, and K. J. Vahala, "Ultra-high-*Q* toroid microcavity on a chip," Nature **421**, 925–928 (2003).
34. T. Asano, B.-S. Song, and S. Noda, "Analysis of the experimental Q factors (~1 million) of photonic crystal nanocavities," Opt. Express **14**, 1996–2002 (2006).
35. D. J. Brady, G. C. Papen, and J. E. Sipe, "Spherical distributed dielectric resonators," J. Opt. Soc. Am. B **10**, 644–657 (1993).
36. M. A. Kaliteevski, S. Brand, R. A. Abram, and V. V. Nikolaev, "Optical eigenmodes of a multilayered spherical microcavity," J. Mod. Opt., **48**, 1503–1516 (2001).
37. Y. Xu, W. Liang, A. Yariv, J. G. Fleming, and S.-Y. Lin, "High-quality-factor Bragg onion resonators with omnidirectional reflector cladding," Opt. Lett. **28**, 2144–2146 (2003).
38. X. H. Zheng, "Theory of two-dimensional 'fingerprint' resonators," Electron. Lett. **25**, 1311–1312 (1989).
39. X. H. Zheng and S. Lacroix, "Mode coupling in circular-cylindrical system and its application to fingerprint resonators," J. Lightwave Technol. **8**, 1509–1516 (1990).
40. D. Englund, I. Fushman, and J. Vučković, "General recipe for designing photonic crystal cavities," Opt. Express **13**, 5961–5975 (2005).
41. J. A. Stratton, *Electromagnetic Theory* (McGraw-Hill, 1941).
42. L. Poladian, F. Ladouceur, and P. D. Miller, "Effects of surface roughness on gratings," J. Opt. Soc. Am. B **14**, 1339–1344 (1997).
43. W. Bogaerts, P. Bienstmann, and R. Baets, "Scattering at sidewall roughness in photonic crystal slabs," Opt. Lett. **28**, 689–691 (2003).
44. Note that, in reality, the coefficients ξ_m^j and η_m^j have units of $\mathrm{V\,m^{-1}}$.
45. M. Abramowitz and I. Stegun, *Handbook of Mathematical Functions with Formulas, Graphs, and Mathematical Tables* (Dover, 1972).
46. R. F. Harrington, *Time-Harmonic Electromagnetic Fields* (McGraw-Hill, 1987).
47. K. Zhang and D. Li, *Electromagnetic Theory for Microwaves and Optoelectronics* (Springer, 1998).
48. I. S. Gradshteyn and I. M. Ryzhik, *Table of Integrals, Series, and Products* (Academic, 1980).
49. G. N. Watson, *A Treatise on the Theory of Bessel Functions* (Cambridge U. Press, 1962).
50. A. Erdélyi, M. F. Oberhettinger, and F. G. Tricomi, *Tables of Integral Transforms. Based, in Part, on Notes Left by Harry Bateman and Compiled by the Staff of the Bateman Manuscript Project* (McGraw-Hill, 1954).
51. It is worth mentioning that finding a suitable physical measure to probe the spectral response of a leaky cavity accordingly is related to a more general issue than expected; in fact, the FWHM estimation of the cavity resonance essentially depends on the technical setup to access the corresponding field quantity and, hence, to the problem of proper normalization (or appropriate excitation) of the cavity mode. Thus the spectrally determined *Q* factors become context dependent. Given the normalization of the wave amplitudes in the cavity center, as proposed by condition (22), the resulting spectral response of the total field energy $\mathcal{W}^m(\lambda)$ yields a physically counterintuitive, but mathematically correct, drop at resonance.
52. *COMSOL Multiphysics*, http://www.comsol.com
53. S. Gulde, A. Jebali, and N. Moll, "Optimization of ultrafast all-optical resonator switching," Opt. Express **13**, 9502–9515 (2005).